Peer review status: This is a non-peer-reviewed preprint submitted to EarthArXiv. The preprint was submitted to Progress in Oceanography for peer review.

Highlights

South Atlantic abyssal temperature variability and trends at 34.5°S

Maurício R. Rocha, Edmo J. D. Campos, Alberto R. Piola, Mathias C. van Caspel, Paulo S. Polito, Cesar B. Rocha

- New records of near-bottom temperature in the South Atlantic show unexpectedly fast warming of abyssal waters;
- The records also display large variability, including a previously unremarked synoptic (4 days) signal;
- Local processes, such as eddies and waves, likely control the synoptic variability.

South Atlantic abyssal temperature variability and trends at 34.5°S

Maurício R. Rocha[a], Edmo J. D. Campos[a], Alberto R. Piola[b], Mathias C. van Caspel[c], Paulo S. Polito[a], Cesar B. Rocha[a]

[a] *Instituto Oceanográfico, Universidade de São Paulo, Brazil*
[b] *Universidad de Buenos Aires, Argentina*
[c] *Alfred-Wegener-Institut Helmholtz-Zentrum für Polar- und Meeresforschung , Germany*

Abstract

Warming of abyssal waters in the South Atlantic has been reported in recent years. However, the variability of bottom temperatures and its implications for assessing linear trends have received limited attention. In addition to confirming positive temperature trends, this study documents substantial bottom-temperature variability, from tidal to annual time scales, captured by bottom moorings deployed at two previously unobserved sites at 34.5°S: Site E (31.13°W, 4007 m) and Site F (18.82°W, 3389 m). The record spans January 2019 to January 2023, with measurements collected every 30 minutes. At each site, temperature sensors were placed approximately 50 m above the seafloor. Both sites exhibit bottom-temperature variance concentrated in the 3–12-month band, consistent with a semiannual cycle, and a dominant semi-diurnal tidal peak. Site E displays an unexpectedly strong signal at ~4-day periods, accounting for ~10% of the total variance, and a larger warming trend (13.0 ± 0.4 m °C yr^{-1}) compared to Site F (4.7 ± 0.2 m °C yr^{-1}). Differences in the temperature variance spectra between sites, along with a wavelet coherence analysis, suggest that local processes (e.g., topographic eddies and internal waves) play a significant role in driving bottom-temperature variability over 2 to 8 days. These results underscore the importance of sustained deep-ocean monitoring to distinguish long-term trends from short-term fluctuations and to elucidate the mechanisms driving bottom-temperature changes in the South Atlantic.

Keywords: Near-bottom temperature, Strong variability, Fast warming, South Atlantic.

1. Introduction

In the South Atlantic, an observational effort began in 2009 with the deployment of an array of Pressure Inverted Echo Sounders (PIES) to measure the Atlantic Meridional Overturning Circulation (AMOC). Located along the 34.5°S, these PIES form the backbone of the South Atlantic Meridional Overturning Circulation (SAMOC) Basin-wide Array (SAMBA) (Ansorge et al., 2014; Manta et al., 2021; Perez et al., 2023; Chidichimo et al., 2023). With the installation of bottom sensors, the array reveals large variability of the AMOC abyssal cell volume transport (Kersale et al., 2020) as well as previously unreported local features of the abyssal circulation in the Southwest Atlantic (Valla et al., 2019).

SAMBA sites were originally distributed on the western and eastern sides of the basin, where the strongest flows are found (See the middle of the triangles in Figure 1). To fill the gap in the middle of the basin, two PIES were installed in January 2019, at 31.13°W (Site E) and 18.82°W (Site F), at depths of 4007 m and 3389 m, respectively (Figure 1). Attached to each PIES was a temperature-conductivity sensor (MicroCAT), approximately 50 m above the seafloor. The MicroCATs were recovered in January 2023.

In the South Atlantic, Antarctic Bottom Water (AABW) and Lower Circumpolar Deep Water (LCDW) dominate the abyssal layers. The AABW forms on Antarctic shelves—mostly in the Weddell Sea—, and spreads northward into the South Atlantic (Carmack and Foster, 1975; Georgi, 1981; Solodoch et al., 2022). Above the AABW is the LCDW, characterized by a salinity maximum and nutrient minima that result from mixing with the overlying North Atlantic Deep Water (NADW) (Whitworth III and Nowlin Jr, 1987; Valla et al., 2018). The LCDW flows equatorward mainly via deep western boundary currents (Onken, 1996; Carter

Email address: mauricio.rocha@usp.br (Maurício R. Rocha)

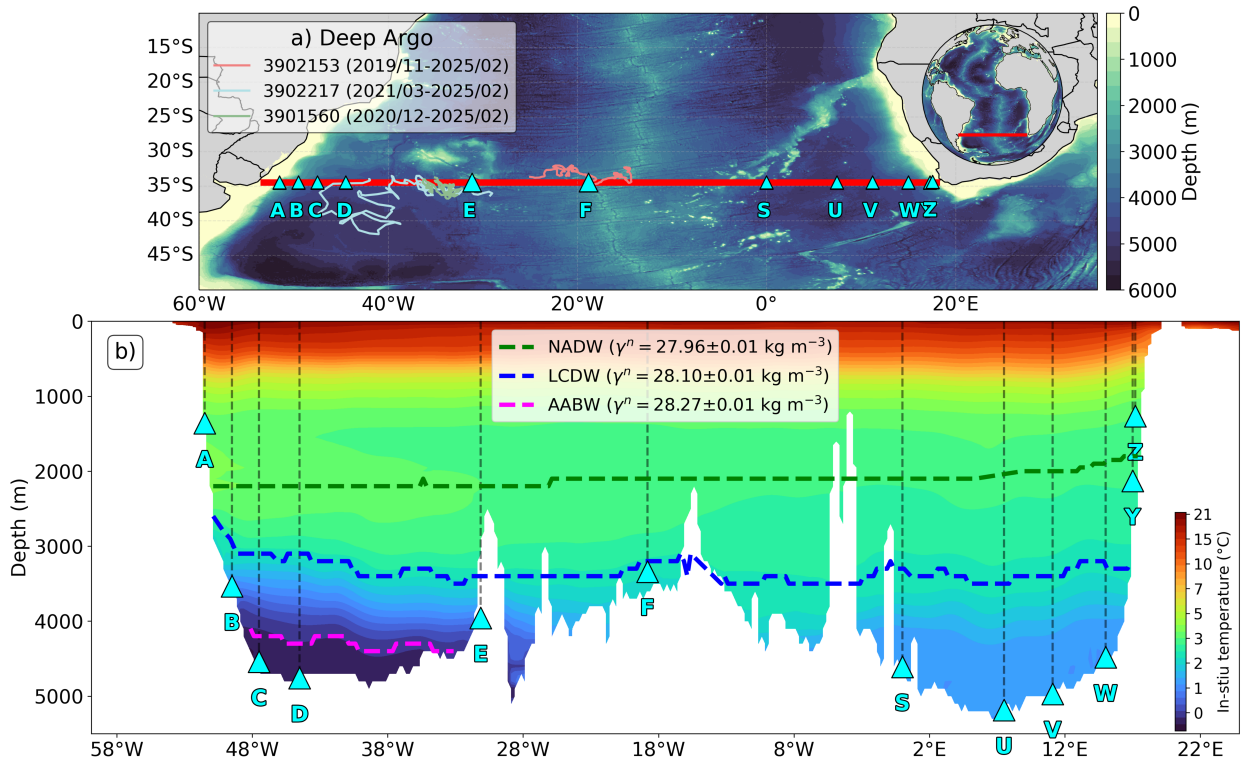

Figure 1: a) Geographic location of the SAMBA array, along 34.5°S in the South Atlantic, with locations of inverted echo sounders shown in triangles and trajectories of deep Argo floats as colored lines. b) Vertical section of in-situ temperature from the World Ocean Atlas 2023 (2015-2022) along the SAMBA line (34.5°S). The upper limits of the Antarctic Bottom Water (AABW), the Lower Circumpolar Deep Water (LCDW), and the North Atlantic Deep Water (NADW) are shown following Valla et al. (2018). The topography is from the World Ocean Atlas; therefore, it is not strictly realistic.

et al., 2008). The combined LCDW/AABW volume transport contributes a large fraction of the deep western boundary current in the Southwest Atlantic (Valla et al., 2019).

Bottom temperature records in the Southern Hemisphere, particularly in the Argentine and Brazil basins, show a consistent warming trend (Coles et al., 1996; Purkey and Johnson, 2010; Herrford et al., 2017; Meinen et al., 2020; Johnson et al., 2020; Campos et al., 2021; Johnson, 2022; Chidichimo et al., 2023; Li et al., 2023; Frey, 2025; Santos et al., 2025). Compared to historical shipboard hydrography (1972-1998), deep-Argo observations (2021-2022) indicate an AABW warming rate of 2.1 m °C yr^{-1} (1 m °C = 10^{-3} °C) (Johnson, 2022). Using new and WOCE-era mooring records combined with CTD casts, Campos et al. (2021) report a similar AABW warming in the Vema Channel, with an increase in the rate observed from 2008 to 2020.

Although the overall warming of abyssal waters in the South Atlantic is now well documented from both observations (Johnson et al., 2020; Campos et al., 2021; Biló et al., 2024; Frey, 2025; Santos et al., 2025) and models (Patara and Böning, 2014; Li et al., 2023), the uncertainties of warming estimates have received far less attention. Valla et al. (2019) showed that uncertainties in the abyssal volume transport at 34.5°S stem primarily from the substantial variability in both velocity records and transport estimates. In the northwest Argentine Basin, Meinen et al. (2020) suggest that energetic variability near the seafloor underscores the need for routine, high-frequency observations to quantify deep and abyssal ocean temperature trends reliably. Moreover, the analysis suggests that yearly observations are necessary to capture the decade long temperature trend to within a 50% error. For bottom temperature in the Drake Passage, Tracey et al. (2017) state that lengths of 13 to 17 years of continuous records are necessary to estimate robust long-term trends. Consequently, short time series or infrequent observations can mask true trends due to the effect of large high-frequency variability.

In this study, we analyze four years of continu-

ous near-bottom temperature records in the middle of the South Atlantic from SAMBA MicroCAT moorings (Sites E and F at 34.5°S, Figure 1). The data reveal previously undocumented, strong synoptic variability (~4 days) and relatively rapid linear warming at Site E. By combining spectral analysis, variance trends, and wavelet-coherence diagnostics, we show that local processes (e.g., topographic eddies, internal waves) dominate the synoptic band, whereas basin-scale seasonal forcing controls the annual signal. These findings highlight the importance of ongoing, high-resolution abyssal monitoring to separate genuine long-term warming from short-term variability and to improve our mechanistic understanding of bottom-temperature variability in the abyssal ocean.

The manuscript is organized as follows. Section 2 describes the datasets and the analysis methods employed. Section 3 presents the basic statistics, linear trends, and spectral analyses of the bottom-temperature records, followed by a discussion of the results. Finally, Section 4 summarizes the main findings and outlines directions for future work.

2. Material and Methods

2.1. Near-bottom temperature records

This study reports near-bottom temperature observations collected at two sites (Figure 1) near 34.5°S in the western South Atlantic. Site E is located at 4007 m south of the Rio Grande Rise (31.13°W) and site F at 3389 m on the western flank of the Mid-Atlantic Ridge (18.82°W). Each site included a Seabird MicroCAT which logged temperature with a precision of 0.1 m °C at 30-minute intervals. Because the conductivity sensors on the MicroCATs drifted, we could not confidently convert the in-situ temperature to conservative temperature due to the lack of reliable salinity records. Nonetheless, tests that assumed a constant salinity to compute conservative temperature produced variability and trends indistinguishable from those derived from the raw in-situ measurements. Consequently, all results—except for comparisons with other datasets in the temperature-salinity (TS) space—are presented using the in-situ temperature data.

To diagnose changes in higher-frequency variability, we calculate the running standard deviation of temperature using moving boxcar windows of 48 points (1 day), 1440 points (30 days), and 8640 points (180 days).

2.2. Ancillary datasets

Because the MicroCATs could not be calibrated immediately before or after deployment, we have compared their measurements with independent datasets. At the same sites and over the same period, two Pressure-Inverted Echo Sounders (PIES) recorded bottom temperatures using an internal thermistor (Meinen et al., 2020). In addition, three deep Argo floats (Argo 3902217, Argo 3901560, and Argo 3902153) traversed the vicinity of Sites E and F (Figure 1). To provide a climatological reference, we extracted values from the latest releases of the World Ocean Atlas (WOA23, 2015–2022) (Reagan et al., 2024; Locarnini et al., 2024) at the grid points closest to Sites E and F. These complementary records provide us with confidence in the MicroCAT temperature series, despite the lack of direct laboratory or factory calibration.

2.3. Linear trend estimates

We estimated the near-bottom temperature linear trend with a standard least-squares regression, expressing the trend in units of ($\mathrm{m\,^{\circ}C\,yr^{-1}}$). The same procedure was applied to the running standard deviation, using a 48-point (1-day), 1440-point (30-day), and 8640-point (180-day) moving window.

To assess the statistical significance of the observed trends, we employed a Monte Carlo approach (Boyle, 1977). For both the temperature and standard-deviation time series we generated 10 000 surrogate series that retain the original mean, variance, and autocorrelation structure but no trend. Each series was subjected to identical least-squares regression analysis, producing a distribution of trend values with a non-zero mean.

The two-sided p-value was computed as the fraction of surrogate slopes whose absolute magnitude equals or exceeds that of the real-data slope. Trends were deemed significant at the 95% confidence level ($p < 0.05$).

2.4. Fourier and wavelet spectral analyses

2.4.1. Frequency spectral analysis

We computed the power spectral density (PSD) of each time series from its discrete Fourier transform. Prior to the transform, the series was detrended, and the sampling interval ($\Delta t = 1800$ s) yields a Nyquist frequency of 2.78×10^{-4} cps.

To reduce noise in the spectral estimates, we smoothed the PSD with a variable-window moving-median filter. The window length is scaled inversely with frequency (i.e., proportional to the period) using a constant smoothing-scale factor, but it is bounded by fixed minimum and maximum sizes to prevent excessive flattening, especially at low frequencies. Confidence intervals for the PSD were derived from the χ^2 distribution, taking into account the

effective number of spectral degrees of freedom from the window-median filter.

We focused our spectral description on two dominant frequency bands because they exhibit the highest PSD: (i) a low-frequency band (3-12 month periods), which captures intra-seasonal, semiannual, and annual variability; and (ii) a higher-frequency band (2-8 days), which captures synoptic-scale processes. The variance explained by these bands in relation to the total signal was calculated using the PSD integral in the frequency domain, following Parseval's theorem. Although tidal frequencies ($\leq$ 1-day) appear prominently in the spectra, we did not treat them as a separate band because this variability is already well documented (Tracey et al., 2017; Meinen et al., 2020; Souza-Neto et al., 2024).

2.4.2. *Wavelet analysis*

Because the statistics of the temperature timeseries are not homogeneous, i.e., the standard deviation shows a trend, we performed a continuous wavelet transform (CWT) analysis (Torrence and Compo, 1998). First, we detrended and normalized the time series by subtracting the mean and dividing by the standard deviation. The CWT employed the Morlet wavelet as the mother wavelet, with a resolvable scale range of 2 to 720 days. Thus, the primary tidal components are not included in the analysis. The cone of influence defined the region where edge effects are negligible, with 95% confidence level (Torrence and Compo, 1998).

To assess statistical significance, we estimated a red noise background spectrum and compared the observed wavelet power against this background spectrum using a χ^2 distribution. Bands in the scalograms that exceed the 95% confidence threshold are highlighted. In addition, we compute the global wavelet spectrum (i.e., the time-averaged wavelet power) and overlain its corresponding significance curve to evaluate which scales are persistent in terms of variability throughout the analyzed period.

Finally, we extracted the scale-averaged time series of the integral of spectral power density for two specific period bands: 2–8-day (synoptic) and 90–365-day (intra-seasonal to annual). For visual comparison between sites, the band-averaged variance was normalized by the maximum value found for Site E.

3. Results and Discussion

3.1. *Comparison of MicroCATs with other temperature records*

Because no CTD profiles were available to calibrate the MicroCATs, we validate their temperature records with independent measurements described in section 2.2. Figure 2 shows a direct comparison of these measurements on a TS diagram. By and large, the MicroCAT temperature at Site F lies within the range spanned by WOA23 climatology (1.85 °C and 35.01 g kg^{-1} at Site F) and deep-Argo floats, supporting the reliability of our in-situ time series. At Site E, the MicroCAT also falls within the range estimates by the deep-Argo floats. However, for this specific location, WOA23 does not reach the depth where the MicroCAT is located, therefore it shows a temperature higher (2.22 °C and 35.04 g kg^{-1}) than the one observed by the MicroCAT.

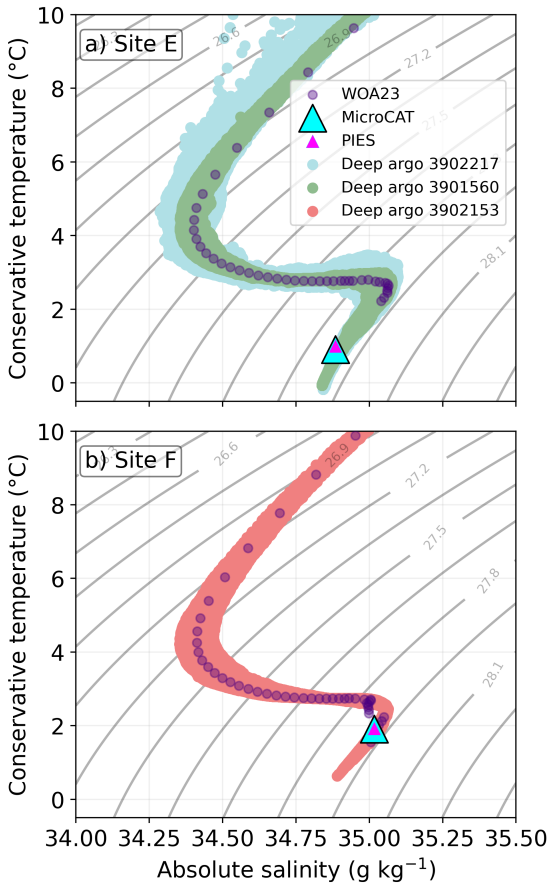

Figure 2: TS diagram for measurements near and at Sites a) E and b) F, where the MicroCATs and PIES were installed. Because the MicroCAT conductivity sensors failed, we computed conservative temperature using salinity from WOA23 (2015–2022). The same approach was applied to the PIES, which also lack conductivity measurements. The deep-Argo float profiles were collected along the trajectories shown in Figure 1a. The PIES and MicroCATs represent a time-averaged value.

The temperature time series at Sites E and F are shown in Figure 3a, b. Linear trends in temperature

and standard deviation at Site E are roughly an order of magnitude larger than those at Site F (Table 1). Although the standard deviation indicates substantial variability, which could mask trends, the linear trends are significant at the 95% confidence level. In particular, the warming trends at Site E exceed by one order of magnitude the rates previously reported in the Vema Channel ($2.6\,\mathrm{m\,^{\circ}C\,yr^{-1}}$) (Campos et al., 2021; Frey, 2025).

Table 1: Statistics of the temperature time series sampled at Sites E and F. The standard deviation of the linear trend is calculated for a moving average with a window size of 48 elements (1-day), 1440 elements (30-day), and 8640 elements (180-day).

	Site E	**Site F**
Record length (days)	1460	1461
Sampling interval (s)	1800	1800
Nominal depth (m)	3956	3338
Mean (°C)	1.2179	2.1823
Median (°C)	1.2286	2.1847
Mode (°C)	1.2661	2.2008
Std. Dev. (°C)	0.1084	0.0514
Min. (°C)	0.8335	2.0252
Max. (°C)	1.5980	2.3417
Linear trend ($\mathrm{m\,^{\circ}C\,yr^{-1}}$)	13.0	4.7
Linear trend uncertainty ($\mathrm{m\,^{\circ}C\,yr^{-1}}$)	0.4	0.2
Std. Dev. Linear trend – 1-day ($\mathrm{m\,^{\circ}C\,yr^{-1}}$)	3.3	-0.4
Std. Dev. Linear trend – 30-day ($\mathrm{m\,^{\circ}C\,yr^{-1}}$)	5.3	-0.6
Std. Dev. Linear trend – 180-day ($\mathrm{m\,^{\circ}C\,yr^{-1}}$)	11.1	-3.0

The maximum temperatures recorded at Sites E and F during 2019–2023 exceed those observed in the northwest Argentine Basin at Sites B, C, and D over the earlier period of 2009–2019 (see site locations in Fig. 1 of Meinen et al., 2020). Moreover, the temperature standard deviation at Site E is roughly an order of magnitude larger than at Site F, indicating substantially greater fluctuations at Site E. Both sites also display standard-deviation values that surpass those reported for neighboring regions in previous studies (Zenk and Hogg, 1997; Zenk, 2008; Zenk and Visbeck, 2013; Campos et al., 2021).

When examined at the higher-frequency band, the temporal trend in standard deviation diverges between the two sites: Site E shows a statistically significant positive trend of $3.3\,\mathrm{m\,^{\circ}C\,yr^{-1}}$, whereas Site F exhibits a slight negative trend of $-0.4\,\mathrm{m\,^{\circ}C\,yr^{-1}}$ over the 2019–2023 interval. The same trend pattern holds for the lower-frequency bands (30-day and 180-day windows), although the magnitudes differ (see Table 1).

3.2. Frequency spectra

Figure 4 shows the frequency spectra for the near-bottom temperature records. At the lowest resolved frequencies, the dominant signal differs between the two sites. The spectrum of Site E exhibits a semiannual peak, whereas Site F has more variance between the semiannual and annual frequencies. Interannual frequencies (around 720 days) also display significant variance, but this should be interpreted with caution because of the relatively short record of 4 years. In essence, we do not have enough record length to make a strong statement.

At the other end of the spectrum, at both sites, the semi-diurnal tidal constituents (M2 and S2) are the most energetic, followed by the diurnal constituent (K1). The dominance of semi-diurnal and diurnal internal tides is consistent with earlier work in the Drake Passage and the South Atlantic (Tracey et al., 2017; Meinen et al., 2020). Site E additionally displays the second-harmonic overtide M4 of the M2 tide, likely reflecting strong internal-tide generation and wave-wave interactions over the steep flank of a nearby seamount, so-called Eastern Rio Grande Rise (Camboa and Rabinowitz, 1984).

At intermediate frequencies, a pronounced 4-day signal appears in the spectrum of Site E (Figure 4a). Such signal is absent at Site F, suggesting that local processes, such as seamount-driven eddies and or waves, may be at play at Site E. On the western edge of the basin, Site B, which is close to the LCDW core and to the boundary current (Figure 1), is also influenced by local processes (Meinen et al., 2020). It has an estimated dominant time scales of variability between 27–38 days for the period 2009-2019, directed impacted by mesoscale variability from the core of the weakly sheared southward flowing Deep Western Boundary Current (Meinen et al., 2017; Valla et al., 2018; Meinen et al., 2020).

We calculated the variance accounted by the two frequency bands highlighted in Figure 4 at each site. At Site E and F, the 2–8-day band accounts for approximately 10.4% and 4.0% of the total variance, respectively. In contrast, 90–365-day frequency contains about 56.7% and 44.2% of the total variance at Sites E and F, respectively. While the dominance of intraseasonal, semiannual, and annual signals was expected (e.g., Meinen et al., 2020), the 10% of total variance concentrated around 4-day is a new finding and a distinctive feature of Site E.

3.3. Wavelet analysis

The standard deviation of temperature at both Sites E and F by far exceeds the linear trend over the 4-year record. Notably, Site E exhibits a positive trend in standard deviation calculated over different windows (Table 1), indicating changes in temperature variability over time. To characterize these non-stationary signals,

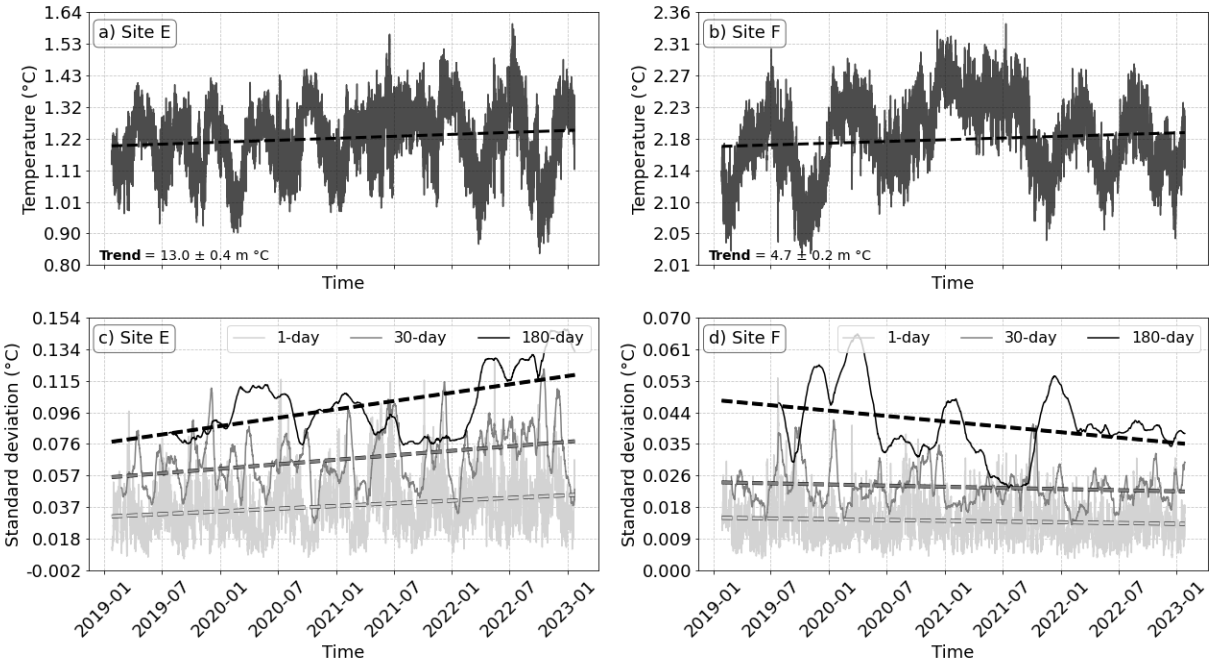

Figure 3: a) and b) Time series of the temperature with fitted linear trend in corresponding color. c) Standard deviation of temperature records at Site E derived from moving-average of 48 points (1 day), 1440 points (30 days), and 8640 points (180 days), each accompanied by its own linear trend line. d) The same set of standard-deviation curves and linear trends lines for Site F.

we performed a wavelet analysis (Torrence and Compo, 1998).

Figure 5 shows the scalograms of the detrended and normalized temperature records, covering periods from 2 days to 2 years, the global wavelet spectrum, and the average variance for the frequency 2–8-day and 90–365-day bands. Those bands have been highlighted previously (See Figure 4). Notably, the cone of influence significance indicates that any signal with periods greater than 1 year should be interpreted with caution. It is necessary to have a few more years of continuous data sampling to make stronger statements about variabilities that fall in that part of the spectrum.

The semiannual cycle emerges as the most prominent signal at Site E and Site F, as previously highlighted in the frequency spectra analysis (Fig. 5b, d). At Site E, the synoptic signal centered around a 4-day period strengthens during the latter half of the record, revealing a locally and temporally dependent near-bottom variability at relatively short time scales (Fig. 5c). The average variance for periods within 2-8 days and 90–365 days differs markedly between the two sites (Figure 5e). In the 2–8-day band, Site E exhibits a higher average variance than Site F, and this variance shows an upward trend over time. In the 90–365-day band—where the bulk of the variance resides at both locations—the variance declines at Site F while it rises at Site E, suggesting a propagation of intra-annual signals between the two sites. The increase (decrease) in variance at Site E (Site F) is consistent with the positive (negative) trend in standard deviation on Site E (Site F) (Table 1).

The SAMBA array is between critical latitudes for the first mode of the baroclinic Rossby waves with 3 and 6 months period (Polito and Sato, 2015). An increase in variance at Site E and a decrease at Site F may indicate a signal propagation from east to west, west of the Mid-Atlantic Ridge. Thus, the subannual signals propagating from Site F to Site E and favoring the increase in variance westwards might be attributed to these waves or even eddies, which commonly ride the Rossby waves at 34.5°S (Polito and Sato, 2015).

To verify the coherence of signals between the two sites, we carried out a wavelet-coherence analysis (Torrence and Webster, 1999; Grinsted et al., 2004). This method identifies common, time-localized oscillations in two time series. The results in Figure 5f show insignificant coherence between the sites for the 4–8-day band, implying that local processes, such as eddies and waves, are likely to control the variability of the synoptic signals.

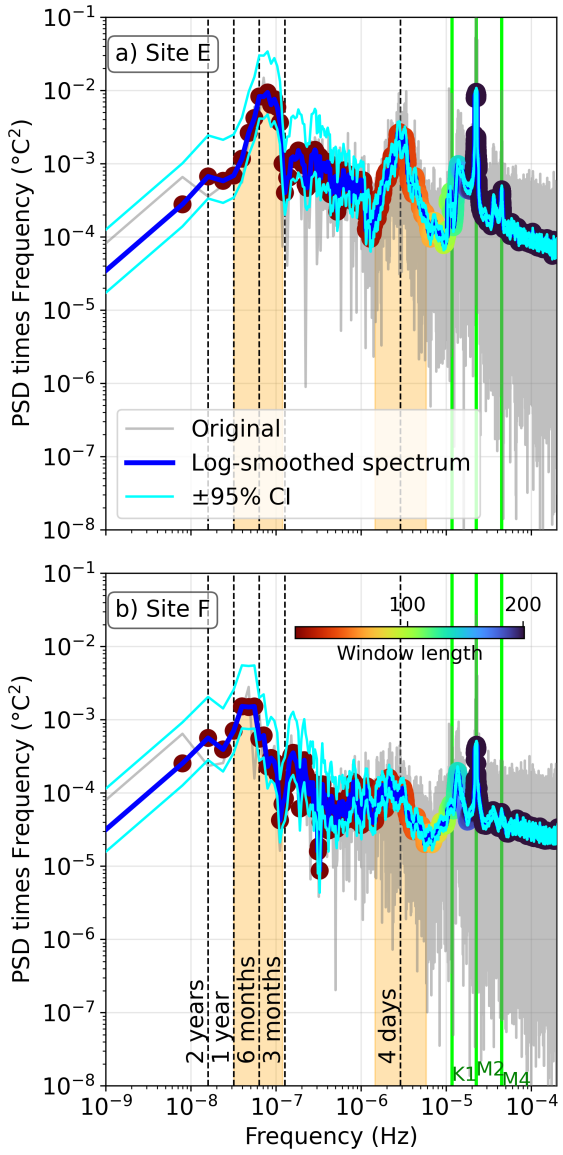

Figure 4: Frequency spectra of temperature variance for a) Site E and b) Site F. The spectra were smoothed with a moving-median filter, taking into account a window length and number of points shown on proportional to frequency (see colorbar). The estimated uncertainty at the 95% confidence interval was computed by considering this window length to determine the number of degrees of freedom in the smoothed spectra. Yellow bands mark low- and high-frequency ranges used for subsequent variance calculations. Green vertical lines denote the tidal constituents M2 (12.42 h), K1 (23.93 h), and M4 (6.21 h).

In contrast, the annual variability presents significant coherence between Sites E and F. For the band centered on the semiannual cycle, a significant correlation between the sites is detected in the second half of the records, with a phase lag between 90-180° of Site F relative to Site E. For the annual cycle, the two sites remain out of phase throughout the record, with Site F leading Site E by 180-270°, suggesting the imprint of seasonal forcing in the near-bottom temperature variability.

Meinen et al. (2020) performed a coherence spectra analysis among SAMBA Sites A, B, C, and D, which are spaced 200-300 km apart (Figure 1). Their results show a little of coherence—generally below 0.5—among the sites, except for the very low-frequency, record-length trends. They remarked that nearly all near-bottom temperature variability in the region occurs at spatial scales smaller than 200-300 km. Our results are consistent with those of Meinen et al. (2020), underscoring the dominant role of local processes, such as mesoscale and submesoscale eddies and waves, in driving the high-frequency (but subinertial) variability of near-bottom temperature.

4. Summary and Conclusions

We analyze the temperature records collected every 30 minutes during 4-year at two previously unobserved sites located near the bottom of the South Atlantic: Site E (31.13°W, 34.5°S, 4007 m) and Site F (31.13°W, 34.5°S, 3389 m). Both moorings lie in the climatological layer of the Lower Circumpolar Deep Water (LCDW). Site F falls very close to the North Atlantic Deep Water (NADW)/LCDW interface. Consequently, the temperature records likely reflect contributions from both the NADW —particularly at Site F— and the Antarctic Bottom Water (AABW)—especially at Site E.

Our analysis documents a pronounced and statistically significant warming of bottom waters, consistent with earlier observations in the Southwest Atlantic (Meinen et al., 2020; Campos et al., 2021). Notably, Site E exhibits a rapid warming rate of 13.0 ± 0.4 m °C yr^{-1}, substantially exceeding previous estimates around 2.6 m °C yr^{-1}.

Near-bottom temperature variability in the region spans a wide range of time scales and exhibits marked heterogeneity throughout the record. Prominent signals occur in the 90–365 day range as well as at around 4-day and the semidiurnal tidal frequency. Within 90–365 days, the variance decreases over time at Site F but increases at Site E. The high variability around 4 days is restricted to Site E, suggesting that local processes drive near-bottom temperature synoptic variability.

Continuous basin-wide temperature records are essential to confirm whether the long-term abyssal warming trends are truly accelerating, as predicted by climate

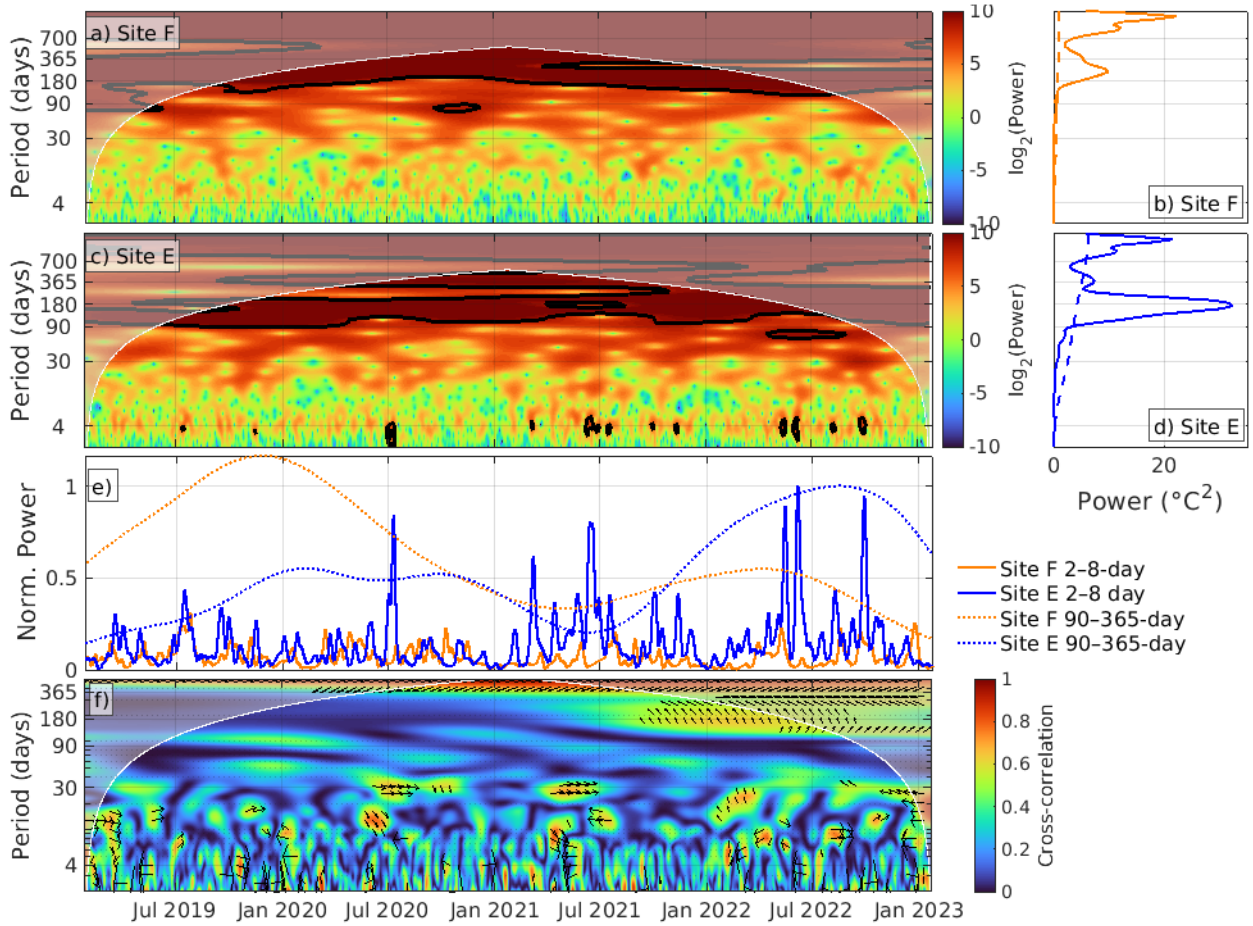

Figure 5: a) Wavelet scalogram of the wavelet transform of the temperature records at Site F, with the cone of influence significant regions highlighted in black. c) Same as a) but for site E. b) and d) Time integral of the scalograms (i.e., frequency spectra) for Sites F and E, respectively. e) Variance time series for different frequency bands: 2-8 days (solid lines) and 90-365 days (dotted lines). f) Cross-correlation between the temperature records of the two sites in the time-period domain. Arrows denote the phase lag of Site F relative to Site E; a vertical arrow marks a $\pi/2$ (quarter-cycle) lag. Only arrows with correlation coefficients ≥ 0.5 are displayed.

models. Our findings have practical implications for deploying abyssal moorings to this end, because strong synoptic to interannual variability may mask long-term warming trends in short records. In addition, given the large variance at a wide range of timescales revealed by the available multi-year near-bottom temperature observations, estimates of the comparatively small long-term trends based on sporadic hydrographic observations must be interpreted with caution.

Credit Authorship Contribution Statement

Maurício R. Rocha: Formal analysis, Data curation, Conceptualization, Investigation, Methodology, Writing – original draft, Visualization, Validation, Writing – review & editing. **Edmo J. D. Campos**: Conceptualization, Funding acquisition, Project administration, Resources, Supervision, Writing – review & editing. **Alberto R. Piola**: Conceptualization, Data curation, Writing – writing & editing. **Mathias C. van Caspel**: Data curation, Investigation. **Paulo S. Polito**: Conceptualization, Methodology, Writing – review & editing. **César B. Rocha**: Conceptualization, Data curation, Formal analysis, Funding acquisition, Investigation, Methodology, Resources, Validation, Visualization, Writing – original draft, Supervision, Writing – review & editing.

Declaration of Competing Interests Statement

The authors declare that they have no known financial or personal conflicts of interest that could have influenced the research reported in this article.

Data Availability

The data will be made available on a publicly accessible platform before the article's final acceptance.

Acknowledgments

This study was supported by the São Paulo Research Foundation (FAPESP; grants 2017/09659-6, 2023/10506-0, 2024/09961-8, and 2024/22376-7) and by Instituto Serrapilheira (grant 2211-41837). We thank the SAMOC Science Team for invaluable discussions, and the Brazilian Navy, Dr. Luiz Nonnato, Eng. Francisco Vicentini and the crew of N. Oc. Antares for their support during the deployment and recovery cruises. We also thank SeCIRM and Petrobras for the fuel oil and DHN for ship time.

References

Ansorge, I., Baringer, M., Campos, E., Dong, S., Fine, R., Garzoli, S., Goni, G., Meinen, C., Perez, R., Piola, A.R., et al., 2014. Basin-wide oceanographic array bridges the south atlantic. Eos, Transactions American Geophysical Union 95, 53–54.

Biló, T.C., Perez, R.C., Dong, S., Johns, W., Kanzow, T., 2024. Weakening of the Atlantic Meridional Overturning Circulation abyssal limb in the North Atlantic. Nature geoscience 17, 419–425.

Boyle, P.P., 1977. Options: A monte carlo approach. Journal of financial economics 4, 323–338.

Camboa, L.A.P., Rabinowitz, P.D., 1984. The evolution of the Rio Grande Rise in the southwest Atlantic Ocean. Marine Geology 58, 35–58.

Campos, E.J., Van Caspel, M.C., Zenk, W., Morozov, E.G., Frey, D.I., Piola, A.R., Meinen, C.S., Sato, O.T., Perez, R.C., Dong, S., 2021. Warming trend in Antarctic Bottom Water in the Vema Channel in the South Atlantic. Geophysical Research Letters 48, e2021GL094709.

Carmack, E.C., Foster, T.D., 1975. On the flow of water out of the Weddell Sea, in: Deep Sea Research and Oceanographic Abstracts, Elsevier. pp. 711–724.

Carter, L., McCave, I., Williams, M.J., 2008. Circulation and water masses of the Southern Ocean: a review. Developments in earth and environmental sciences 8, 85–114.

Chidichimo, M., Perez, R., Speich, S., Kersalé, M., Sprintall, J., Dong, S., Lamont, T., Sato, O., Chereskin, T., Hummels, R., et al., 2023. Energetic overturning flows, dynamic interocean exchanges, and ocean warming observed in the South Atlantic, Commun. Earth Environ., 4, 10.

Coles, V.J., McCartney, M.S., Olson, D.B., Smethie Jr, W.M., 1996. Changes in Antarctic Bottom Water properties in the western South Atlantic in the late 1980s. Journal of Geophysical Research: Oceans 101, 8957–8970.

Frey, D., 2025. Branching of Antarctic Bottom Water flow in the middle part of the Vema Channel revealed by direct velocity measurements. Journal of Geophysical Research: Oceans 130, e2024JC021580.

Georgi, D.T., 1981. Circulation of bottom waters in the southwestern South Atlantic. Deep Sea Research Part A. Oceanographic Research Papers 28, 959–979.

Grinsted, A., Moore, J.C., Jevrejeva, S., 2004. Application of the cross wavelet transform and wavelet coherence to geophysical time series. Nonlinear processes in geophysics 11, 561–566.

Herrford, J., Brandt, P., Zenk, W., 2017. Property changes of deep and bottom waters in the Western Tropical Atlantic. Deep Sea Research Part I: Oceanographic Research Papers 124, 103–125.

Johnson, G.C., 2022. Antarctic Bottom Water warming and circulation slowdown in the Argentine Basin from analyses of Deep Argo and historical shipboard temperature data. Geophysical Research Letters 49, e2022GL100526.

Johnson, G.C., Cadot, C., Lyman, J.M., McTaggart, K.E., Steffen, E.L., 2020. Antarctic Bottom Water warming in the Brazil basin: 1990s through 2020, from WOCE to deep argo. Geophysical Research Letters 47, e2020GL089191.

Kersale, M., Meinen, C.S., Perez, R.C., Le Henaff, M., Valla, D., Lamont, T., Sato, O., Dong, S., Terre, T., van Caspel, M., et al., 2020. Highly variable upper and abyssal overturning cells in the South Atlantic. Science advances 6, eaba7573.

Li, Q., England, M.H., Hogg, A.M., Rintoul, S.R., Morrison, A.K., 2023. Abyssal ocean overturning slowdown and warming driven by Antarctic meltwater. Nature 615, 841–847.

Locarnini, R.A., Mishonov, A.V., Baranova, O.K., Reagan, J.R., Boyer, T.P., Seidov, D., Wang, Z., Garcia, H.E., Bouchard, C., Cross, S.L., et al., 2024. World Ocean Atlas 2023, volume 1: Temperature. NOAA Atlas NESDIS .

Manta, G., Speich, S., Karstensen, J., Hummels, R., Kersalé, M., Laxenaire, R., Piola, A., Chidichimo, M.P., Sato, O.T., Cotrim da Cunha, L., et al., 2021. The South Atlantic meridional overturning circulation and mesoscale eddies in the first GO-SHIP section at 34.5°S. Journal of Geophysical Research: Oceans 126, e2020JC016962.

Meinen, C.S., Garzoli, S.L., Perez, R.C., Campos, E., Piola, A.R., Chidichimo, M.P., Dong, S., Sato, O.T., 2017. Characteristics and causes of Deep Western Boundary Current transport variability at 34.5 S during 2009–2014. Ocean Science 13, 175–194.

Meinen, C.S., Perez, R.C., Dong, S., Piola, A.R., Campos, E., 2020. Observed ocean bottom temperature variability at four sites in the northwestern Argentine Basin: Evidence of decadal deep/abyssal warming amidst hourly to interannual variability during 2009–2019. Geophysical Research Letters 47, e2020GL089093.

Onken, R., 1996. The spreading of Lower Circumpolar Deep Water in the Atlantic Ocean. Oceanographic Literature Review 8, 754.

Patara, L., Böning, C.W., 2014. Abyssal ocean warming around Antarctica strengthens the Atlantic overturning circulation. Geophysical Research Letters 41, 3972–3978.

Perez, R., Garzoli, S., Hummels, R., Ansorge, I., 2023. Inclusive science in the South Atlantic. Communications Earth & Environment 4, 11.

Polito, P.S., Sato, O.T., 2015. Do eddies ride on Rossby waves? Journal of Geophysical Research: Oceans 120, 5417–5435.

Purkey, S.G., Johnson, G.C., 2010. Warming of global abyssal and deep Southern Ocean waters between the 1990s and 2000s: Contributions to global heat and sea level rise budgets. Journal of Climate 23, 6336–6351.

Reagan, J.R., Seidov, D., Wang, Z., Dukhovskoy, D., Boyer, T.P., Locarnini, R.A., Baranova, O.K., Mishonov, A.V., Garcia, H.E., Bouchard, C., et al., 2024. World Ocean Atlas 2023, Volume 2: Salinity. NOAA Atlas NESDIS .

Santos, D.M., Biló, T.C., Napolitano, D.C., Perez, R.C., Polito, P.S., Gula, J., Dong, S., Campos, E.J., Sato, O.T., 2025. Antarctic bottom water contraction drives abyssal ocean warming along SAMBA-West line (34.5° S) in the Argentine basin. Deep Sea Research Part I: Oceanographic Research Papers , 104627.

Solodoch, A., Stewart, A., Hogg, A.M., Morrison, A., Kiss, A., Thompson, A., Purkey, S., Cimoli, L., 2022. How does Antarctic

Bottom Water cross the Southern Ocean? Geophysical Research Letters 49, e2021GL097211.
Souza-Neto, P.W., da Silveira, I.C., Rocha, C.B., Lazaneo, C.Z., Calil, P.H., 2024. The Rio Grande Rise circulation: Dynamics of an internal tide conversion hotspot in the Southwestern Atlantic. Progress in Oceanography 224, 103264.
Torrence, C., Compo, G.P., 1998. A practical guide to wavelet analysis. Bulletin of the American Meteorological society 79, 61–78.
Torrence, C., Webster, P.J., 1999. Interdecadal changes in the ENSO–monsoon system. Journal of Climate 12, 2679–2690.
Tracey, K.L., Donohue, K.A., Watts, D.R., 2017. Bottom Temperatures in Drake Passage. Journal of Physical Oceanography 47, 101–122.
Valla, D., Piola, A.R., Meinen, C.S., Campos, E., 2018. Strong mixing and recirculation in the northwestern Argentine Basin. Journal of Geophysical Research: Oceans 123, 4624–4648.
Valla, D., Piola, A.R., Meinen, C.S., Campos, E., 2019. Abyssal transport variations in the Southwest South Atlantic: first insights from a long-term observation array at 34.5°S. Geophysical Research Letters 46, 6699–6705.
Whitworth III, T., Nowlin Jr, W.D., 1987. Water masses and currents of the Southern Ocean at the Greenwich Meridian. Journal of Geophysical Research: Oceans 92, 6462–6476.
Zenk, W., 2008. Temperature fluctuations and current shear in Antarctic Bottom Water at the Vema Sill. Progress in Oceanography 77, 276–284.
Zenk, W., Hogg, N., 1997. Warming trend in Antarctic Bottom Water flowing into the Brazil Basin. Oceanographic Literature Review 7, 664.
Zenk, W., Visbeck, M., 2013. Structure and evolution of the abyssal jet in the Vema Channel of the South Atlantic. Deep Sea Research Part II: Topical Studies in Oceanography 85, 244–260.

Appendix A

In this section, we repeat the time-series analysis using the internal sensor of the PIES (Meinen et al., 2017, 2020) collected at the same sites where the MicroCATs were installed, during approximately the same measurement periods. Figure A.6 shows the PIES temperature records at Sites E and F, similar to Figure 3. Figure A.6 also presents the linear trends the standard deviation computed using different moving-average windows. The trends from the PIES records are of the same order of magnitude as those from the MicroCATs. The increase of temperature variability at Site E and decrease at Site F over time are also observed in the PIES records.

Figure A.7 shows the frequency spectra for the near-bottom temperature records from the PIES, similar to Figure 4. At the highest resolved frequencies, the spectra differ because the PIES records have a temporal resolution of 60 min, whereas the MicroCATs have a temporal resolution of 30 min and because the PIES house their temperature sensors inside a glass sphere, which likely buffers the signals of fast water temperature variability. For longer periods ($\geq$ 1 day), the PIES and MicroCATs records have similar spectra.

These comparisons lend confidence to the results derived from the MicroCAT temperature records analyzed in this study. In particular, it is unlikely that the trend and associated variability presented here are artifacts of calibration errors or sensor drift in the MicroCAT instruments.

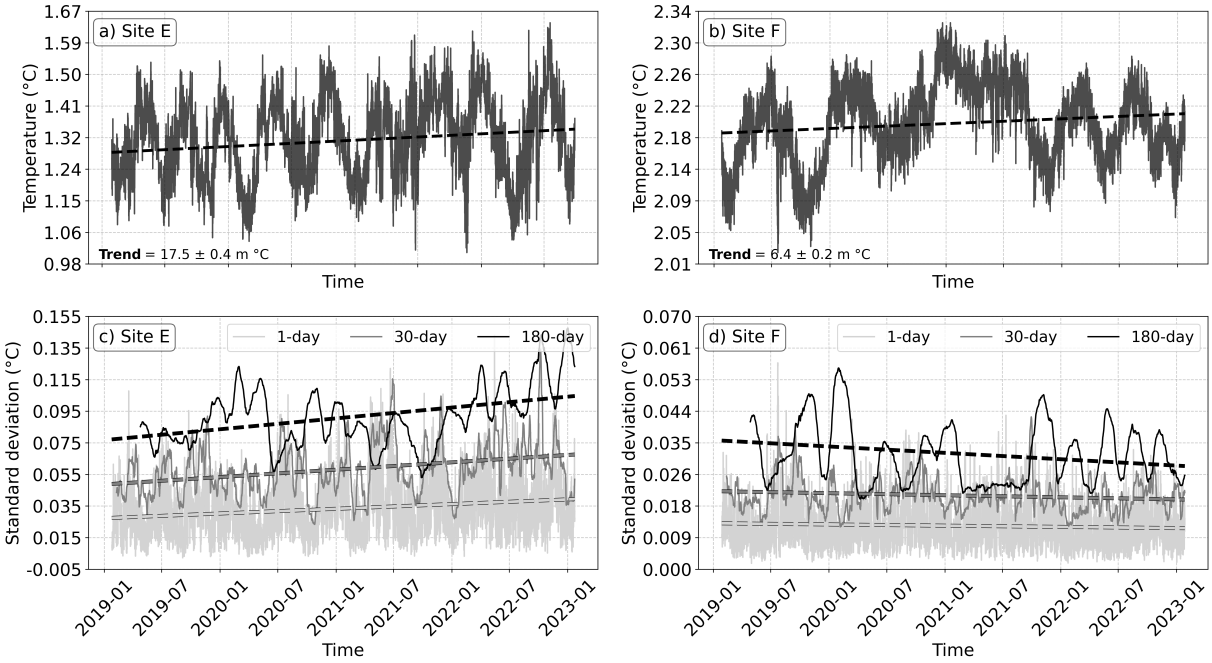

Figure 6: a) and b) Time series of the temperature with fitted linear trend in corresponding color from PIES temperature records, with temporal resolution of 60 min. c) Standard deviation of temperature records at Site E derived from moving averages of 24 points (1 day), 720 points (30 days), and 4320 points (180 days), each accompanied by its own linear trend line. d) The same set of standard-deviation curves and linear trend lines for Site F.

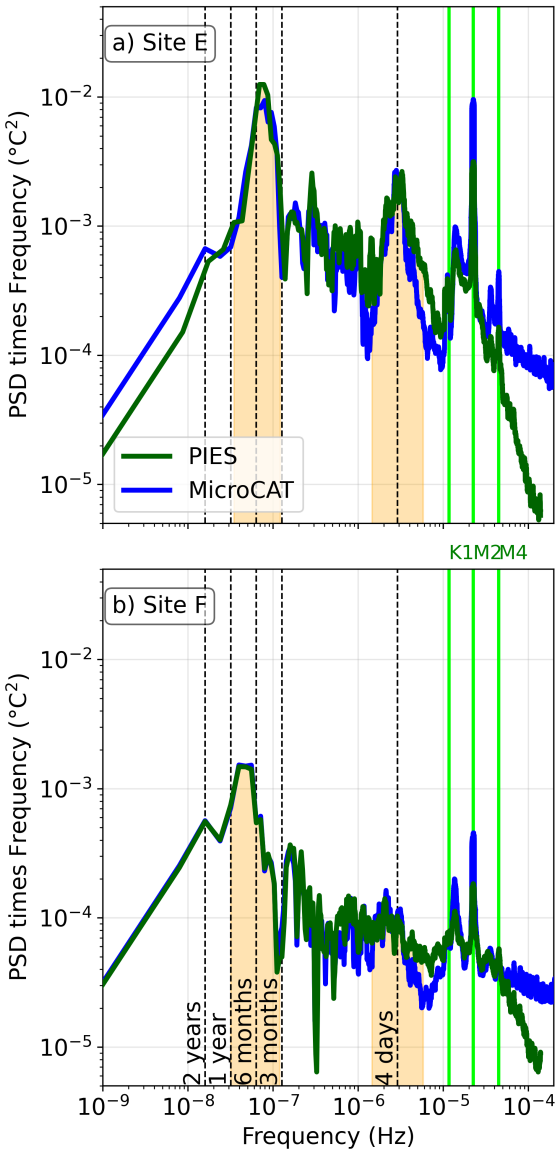

Figure 7: Frequency spectra of temperature variance for a) Site E and b) Site F from PIES and MicroCATs. The spectra were smoothed with a moving-median filter, taking into account a window length and number of points shown on proportional to frequency. Yellow bands mark low- and high-frequency ranges used for subsequent variance calculations. Green vertical lines denote the tidal constituents M2 (12.42 h), K1 (23.93 h), and M4 (6.21 h).